PERGAMON

Computers in Biology and Medicine 31 (2001) 365–384

Computers in Biology and Medicine

www.elsevier.com/locate/compbiomed

Computational particle-hemodynamics analysis and geometric reconstruction after carotid endarterectomy

S. Hyun[a], C. Kleinstreuer[a,*], J.P. Archie Jr[a,b]

[a] *Department of Mechanical and Aerospace Engineering, North Carolina State University, Campus Box 7910, 3211 Broughton Hall, Raleigh, NC 27695-7910, USA*

[b] *Wake Medical Center, Raleigh, NC, USA*

Received 9 June 2000; accepted 29 January 2001

Abstract

Transient three-dimensional laminar incompressible dilute suspension flow in rigid in-plane carotid artery bifurcations has been solved with a user-enhanced finite-volume program. Instantaneous velocity vector and wall shear stress vector fields illustrate strong "disturbed flow" patterns. Implications of elevated surface contours of hemodynamic wall parameters, indicating such disturbed flows, and particle deposition sites are discussed and a relative comparison in terms of indicator functions between the endarterectomized carotid artery bifurcation and two design improvements is shown. Although the combined perioperative mortality and non-fatal stroke rate for carotid endarterectomy ranges only from 2% to 7%, the final geometric design recommendation presented merits consideration because it may significantly lower the chances of post-operative complications such as stroke, ischemic attack, or even death. The new carotid artery bifurcation design is based on the overall reduction of "disturbed flow" indicator functions, including the time-averaged wall shear stress angle deviation and a wall deposition parameter for critical blood particles, such as monocytes.

Keywords: Endarterectomized carotid artery; Particle-hemodynamics simulations; Indicator functions; Surgical reconstruction geometries

1. Introduction

Carotid endarterectomy for stroke prevention has a relatively low but significant incidence of early post-operative thrombosis and early and late restenosis due to intimal hyperplasia and/or recurrent atherosclerosis [1,2]. Operative failures are due in part to the local "disturbed blood flow" patterns and the reconstruction technique [3]. The aggravating hemodynamics in branching blood vessels can be expressed in terms of indicator functions which, for the most part, are based on the local wall

* Corresponding author. Tel.: +1-919-515-5261; +1-919-515-7968.
E-mail address: ck@eos.ncsu.edu (C. Kleinstreuer).

0010-4825/01/$ - see front matter
PII: S0010-4825(01)00007-5

shear stress [4]. In turn, reduction of suitable indicator functions via geometric design changes should delay, or perhaps prevent, the recurrence of arterial diseases. In carotid endarterectomy, the diseased intima and media are removed and the artery is reconstructed, usually via patch angioplasty. Even so, endarterectomy frequently leaves an asymmetric step expansion in the common carotid artery. Patch angioplasty is a practical means to reconstruct the bifurcation geometry according to design recommendations obtained from virtual prototyping [5].

The hemodynamics of carotid artery bifurcations have been analyzed, assuming steady flow [6], pulsatile flow [7], and compliant walls [8]. Possible correlations between indicator functions and intimal thickening in the carotid artery bifurcation have been discussed by Ku et al. [9] and Wells et al. [7]. Geometric effects, such as bifurcation angle and wall curvature, on the hemodynamics were simulated by Perktold et al. [10] and Kleinstreuer et al. [11].

In this paper, focusing on three endarterectomized carotid artery bifurcations and a near optimized carotid artery bifurcation geometry, the wall shear stress angle deviation, its spatial gradient and particle deposition patterns are employed as powerful indicator functions to generate near-optimal design recommendations for surgical reconstruction of endarterectomized carotid artery bifurcations. The results of the computer optimization processes should lead to an improved, generally accepted surgical technique of carotid endarterectomy reconstruction.

2. Theory

The chain of events and underlying hypotheses leading to recommendations for surgical reconstruction of branching arteries are outlined in Fig. 1. Guided by laboratory studies and clinical observations, the desired outcome are surgically reconstructed or manufactured blood vessels with high sustained patency rates. Thus, the first step is the accurate simulation of blood flow in a representative endarterectomized carotid artery bifurcation with realistic inlet and outlet flow waveforms (cf. Fig. 2).

2.1. Governing equations

Assuming laminar incompressible flow of a non-Newtonian fluid and a dilute suspension of spherical particles, e.g., monocytes with $d_p \approx 14$ μm and a density of 1.07 g/cm^3, the governing equations for fluid and particle motion are [12,16]

$$\nabla \cdot \boldsymbol{v} = 0, \tag{1}$$

$$\frac{\partial \bar{v}}{\partial t} + (\boldsymbol{v} \cdot \nabla)\boldsymbol{v} = \frac{1}{\rho}(-\nabla p + \nabla \cdot \boldsymbol{\tau}) \tag{2}$$

and

$$\left(m_p + \frac{m}{2}\right) \frac{\hat{d}^2 \boldsymbol{x}_p}{\hat{d}t^2} = \frac{\pi}{8} \rho\, d_p^2 C_D(\boldsymbol{v} - \boldsymbol{v}_p)|\boldsymbol{v} - \boldsymbol{v}_p|. \tag{3}$$

The non-Newtonian blood rheology used in Eq. (2) is represented by

$$\boldsymbol{\tau} = 2\eta(II_D)\mathbf{D} \tag{4}$$

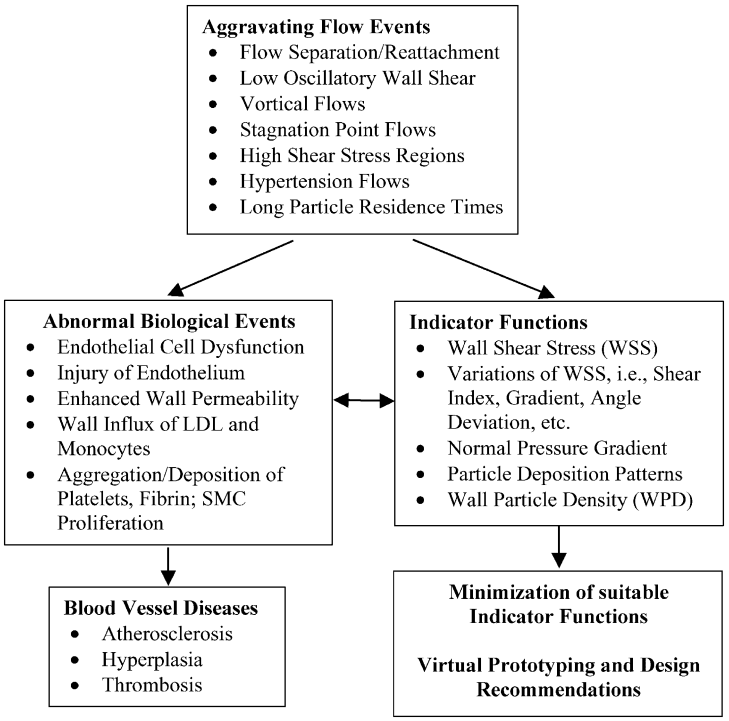

Fig. 1. Flow chart of physico-biological events and methodology for virtual prototyping.

where $\mathbf{D} = \frac{1}{2}[\nabla\bar{v} + (\nabla\bar{v})^{\mathrm{T}}]$, while $\gamma = 2\mathbf{D}$ and η is a function of the shear rate given by an extended Casson model [13] as

$$\eta(II_D) = \frac{1}{2\sqrt{II_D}}[C_1(\mathrm{Ht}) + C_2(\mathrm{Ht})\sqrt{2\sqrt{II_D}}]^2, \tag{5}$$

where

$$II_D = \frac{1}{2}p(\mathrm{tr}\,\boldsymbol{D})^2 + \mathrm{tr}(\boldsymbol{D})^2]. \tag{6}$$

The coefficients C_1 and C_2 in Eq. (5) were determined for a hematocrit of Ht = 40% as $C_1 = 0.2$ (dyn/cm^2)$^{1/2}$ and $C_2 = 0.18$ (dyn s/cm^2)$^{1/2}$ based on Merrill's experimental data [14]. The asymptotic value of the viscosity for a hematocrit of Ht = 40% was taken as the Newtonian viscosity $\mu = 0.0348$ dyn s/cm^2, which guarantees a smooth transition from the Casson model to a Newtonian fluid. Since the Casson model is only suitable for shear rates $\dot{\gamma} > 1$ (s^{-1}), we take $\eta = 0.1444$ dyn s/cm^2 when $\dot{\gamma} < 1$ (s^{-1}), which is the "zero-shear rate" condition. All the values given are at 37°C.

The particle drag coefficient used in Eq. (3) is represented by

$$C_D = 24/\mathrm{Re}_{\mathrm{p}} \quad \text{with } \mathrm{Re}_{\mathrm{p}} = |\boldsymbol{v} - \boldsymbol{v}_{\mathrm{p}}|d_0/v_0. \tag{7a,b}$$

With particle Reynolds numbers $\mathrm{Re}_{\mathrm{p}} \leqslant 1.0$ and very small Stokes numbers, particle motion is basically a first-order correction to fluid-element motion. A particle is declared "deposited" (i) when

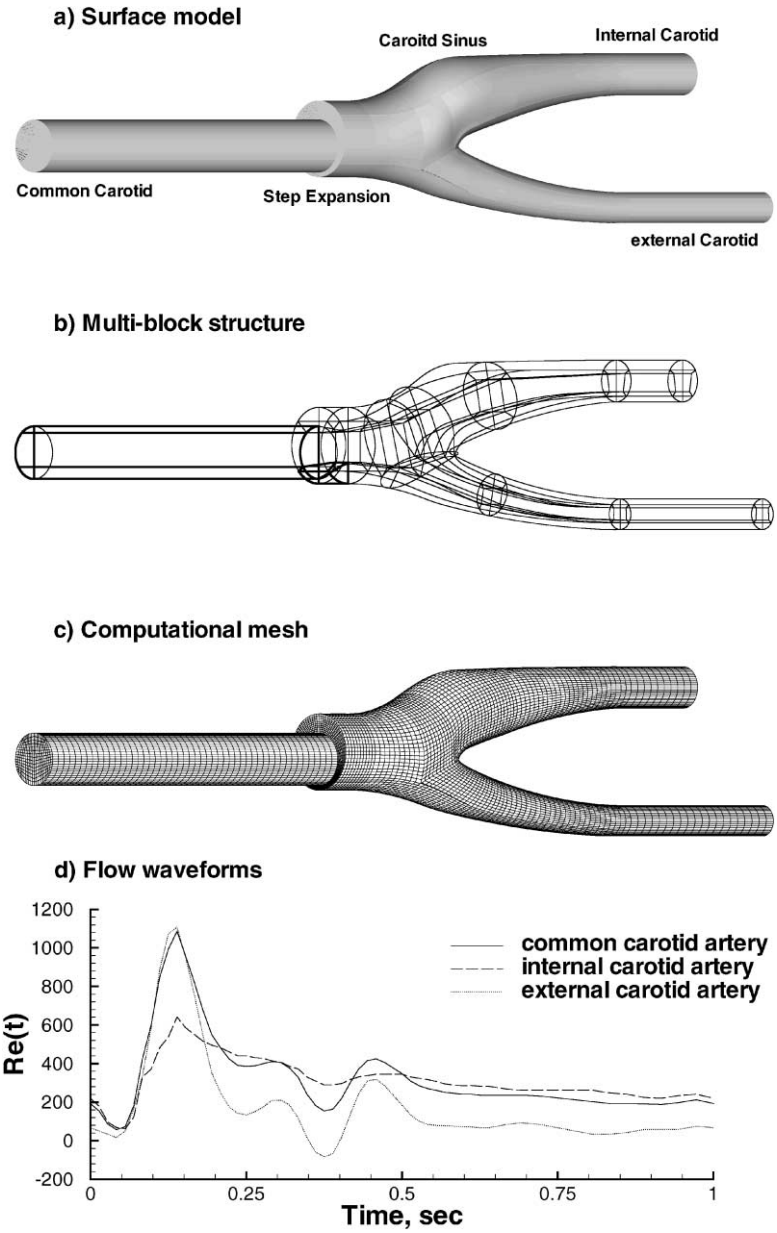

Fig. 2. System schematics: (a) surface model; (b) multi-block structure; (c) computational mesh; and (d) flow waveforms for the endarterectomized carotid artery bifurcation (ECAB).

it is locally about one diameter near the wall, and (ii) when the particle has a measurable normal velocity, $v_{p,n}$, towards the wall, relative to its tangential velocity component, $v_{p,t}$. Specifically, $v_{p,n}|_{n=ad_p} \geqslant bv_{p,t}$ where $a = O(1)$ and $b = O(10^{-1})$; i.e., in the present case study $a = 1$ and $b = 0.5$. To predict the particle motion in pulsatile blood flow, a Lagrangian approach is employed. The

trajectory of a particle suspended by the fluid flow is governed by the rate of change of momentum and the external forces acting upon it (cf. Eq. (3)). The basic assumptions for the particle motion analysis include non-interacting solid spheres as well as negligible pressure gradient force and Basset force. Due to the pulsatility of the blood flow, it is assumed that the particle motion is governed by the drag force and the particle acceleration effect, where m_p is the particle mass, m is the mass of the fluid occupied by the particle, ρ_p is the particle density, d_p is the particle diameter, $\boldsymbol{v}$ is the fluid velocity where the particle center is, and $\boldsymbol{v}_p$ is the particle velocity.

Typical indicator functions include the time-averaged wall shear stress (WSS) [4], wall shear stress gradient (WSSG) [4], oscillatory shear index (OSI) [9], wall shear stress angle deviation (WSSAD) [5,16,17], and wall particle deposition (WPD). At any point i [4,15,16]:

$$\boldsymbol{\tau} \Rightarrow \boldsymbol{\tau}_{w,i} = (\tau_{w,x}, \tau_{w,y}, \tau_{w,z})_i \quad \text{and} \quad \bar{\boldsymbol{\tau}}_{w,i} = \mathrm{WSS} = \frac{1}{T}\int_0^T |\boldsymbol{\tau}_{w,i}|\,\mathrm{d}t. \tag{8a,b}$$

The other indicator functions are defined as

$$\mathrm{WSSG} = \frac{1}{T}\int_0^T |\mathrm{WSSG}|\,\mathrm{d}t, \quad \text{where } |\mathrm{WSSG}| = \left[\left(\frac{\partial \tau_{i,m}}{\partial m}\right)^2 + \left(\frac{\partial \tau_{i,n}}{\partial n}\right)^2\right]^{1/2} \tag{9a,b}$$

$$\mathrm{OSI} = \frac{1}{2}\left(1 - \frac{|\int_0^T \tau_w\,\mathrm{d}t|}{\int_0^T |\tau_w|\,\mathrm{d}t}\right) \tag{10}$$

and

$$\mathrm{WSSAD} = Ca\cos\left(\frac{\bar{\boldsymbol{\tau}}_i \cdot \bar{\boldsymbol{\tau}}_j}{|\bar{\boldsymbol{\tau}}_i| \cdot |\bar{\boldsymbol{\tau}}_j|}\right), \tag{11a,b}$$

where T is the period of the cycle, τ_i is the instantaneous wall shear stress vector, and

$$C = \begin{cases} 1.0 \text{ for } \bar{\boldsymbol{v}}_{n,i}\boldsymbol{n}_i \geqslant 0 \\ 0.0 \text{ for } \bar{\boldsymbol{v}}_{n,i}\boldsymbol{n}_i < 0 \end{cases} \quad \text{and} \quad \bar{\boldsymbol{\tau}}_i = \frac{1}{T}\int_o^T \boldsymbol{\tau}_i\,\mathrm{d}t. \tag{12a,b}$$

The WSSAD is non-zero when the local time-averaged WSS-vector at node i differs from the WSS-vector direction at neighboring nodes $j = 1 \ldots 4$, and when there is no fluid motion away from the wall. For any elapsed time interval, the wall particle density function assesses quantitatively the deposition patterns in major segments of branching blood vessels; here, the common, internal, and external carotid arteries.

The wall particle deposition (WPD) expresses the mass of deposited particles in a well-defined vessel segment during time interval Δt, where, for example, $\Delta t = T$ is for one cycle or $\Delta t \to \infty$, say, $10T$, yields the quasi-equilibrium deposition.

$$\mathrm{WPD} = \frac{1}{\Delta t}\int_0^{\Delta t}\left[\frac{1}{A_s}\iint_A n_p m_p\,\mathrm{d}A\right]\mathrm{d}t, \tag{13}$$

where A_s is the regional surface area, m_p is the mass of a single particle, and n_p is the number of deposited particles.

The segmentally area-averaged indicator functions can be obtained from the time-averaged indicator functions, i.e., Eqs. (9)–(13), as follows:

$$\mathrm{WSSG}_{A_s} = \frac{1}{A_s}\iint_{A_s} \mathrm{WSSG}\,\mathrm{d}A_s$$

$$\mathrm{OSI}_{A_s} = \frac{1}{A_s}\iint_{A_s} \mathrm{OSI}\,\mathrm{d}A_s$$

$$\mathrm{WSSAD}_{A_s} = \frac{1}{A_s}\iint_{A_s} \mathrm{WSSAD}\,\mathrm{d}A_s$$

$$\mathrm{WPD}_{A_s} = \frac{\mathrm{WPD}}{m_p n_{p,\mathrm{in}}} \tag{14a–b}$$

where $n_{p,\mathrm{in}}$ is the total number of inlet particles in the common carotid artery at time $t=0$ s. Thus, the WPD_{A_s} expresses the mass fraction of locally deposited particles. Which indicator function works best for all systems as both a predictor of arterial disease sites and geometric design parameter (cf. Fig. 1), is still somewhat an open question. Ultimately it can only be fully answered through further case-by-case experimental studies and clinical observations. However, for endarterectomized carotid artery bifurcations, Hyun [17] suggested primarily the WSSAD as the best indicator function, with the particle deposition patterns or equilibrium WPD_{A_s} as a supportive parameter. Hyun [17] based his conclusions on parametric sensitivity analyses, medical literature data, and laboratory observations. Furthermore, Buchanan et al. [18,19] showed good agreement between areas of elevated wall permeability and early lesion growth when compared to the WSSAD alone and the WSSG in conjunction with low WSS regions at the junction of the rabbit's aorta–celiac branch.

2.2. Numerical method

Proper mesh generation is a critical task in computational fluid dynamics analysis. For a structured mesh, the domain is subdivided into multiple blocks which are composed of irregular finite volumes, e.g., hexahedrons. In employing CFX 4.2 (AEA Technology, Bethel Park, PA), which incorporates a surface model and mesh generator MESHBUILD, complex surface curvatures and junction boundaries can be readily incorporated while avoiding cell distortion. The use of a locally body-fitted curvilinear system allows for an accurate mapping of complex flow domains (cf. Fig. 2a–c).

The transport equations (1) and (2) with (4)–(6) are integrated over each control volume where the continuity equation (1) is replaced by a pressure-correction equation (SIMPLEC algorithm). The convection coefficients are obtained with the Rhie–Chow interpolation formula in conjunction with a standard upwind technique [20]. The resulting discretized equations are solved iteratively at two levels: an inner iteration to solve for the spatial coupling of each variable and an outer iteration to solve for the coupling between variables. The convergence of the iterations, $\varepsilon \leqslant 10^{-4}$, is controlled by the mass source residual in concert with the velocity, i.e., momentum residual [17].

The particle trajectory equation (3) is solved once the velocity field has been obtained. This initial value problem is solved by using a fourth-order Runge–Kutta method or, alternatively, by another ODEPACK module (cf.) http://www.netlib.org/odepack). The main task is to compute the local (fluid

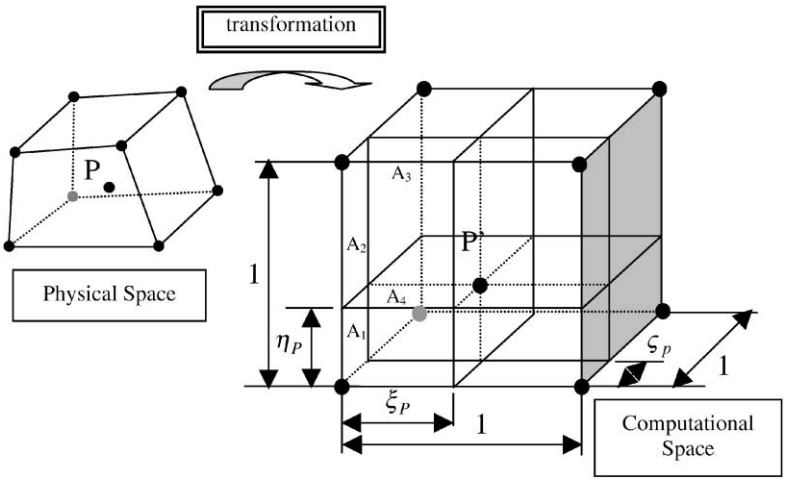

Fig. 3. Coordinate transformation for particle transport calculations.

element) velocity accurately in order to convect each particle faithfully. Specifically, the position of a particle inside an irregular hexahedron in physical space is transformed into a three-dimensional $1 \times 1 \times 1$-cuboid in computational space (cf. Fig. 3). Using the calculated particle position in the computational space (ξ_p, η_p, ζ_p), and vertices information, the sub-divisions of a control volume can be made. Now, the fluid element velocity at the position of a particle can be interpolated using a Lagrange polynomial, which implies volume-weighted averaging for three-dimensional systems. After the velocity has been calculated at the particle location, a new position of the particle can be obtained from integration of Eq. (3) as outlined in more detail by Hyun [17]. The indicator functions, i.e., Eqs. (9)–(14), are evaluated with user-supplied FORTRAN programs [16,17]. The computational work has been performed on a Sun Ultra 30/300 with 512 MB RAM as well as on a Cray T90 and took about 6.0 and 3.5 CPU hours, respectively.

The representative inlet and outlet conditions for the fully developed velocity calculations are depicted in Fig. 2d in terms of transient Reynolds numbers for all three conduits [21], where $Re(t) = \bar{u}(t)d_0/\nu_o$. The tubes are long enough to generate developed axial velocity profiles.

2.3. Computer model validations

The software package CFX 4, the particle trajectory algorithm, and the user-enhanced FORTRAN programs for pre- and post-processing have been validated numerous times with experimental data sets as documented in detail elsewhere [15–17,22–24]. Two examples are shown in Figs. 4 and 5. The computational results of steady flow in the model carotid artery bifurcation are compared to the experimental measurements done by Bharadvaj et al. [6]. The shape of the region with reverse axial flow in the plane of symmetry as well as the axial velocity plateau is matched well by the computational simulation. The critical sites as predicted by the indicator functions are shown in Fig. 5 where the measured intimal thickness lies in the symmetry plane [25]. Larger intimal thickness is found in the region at the non-divider wall in the distal carotid sinus and near the flow divider.

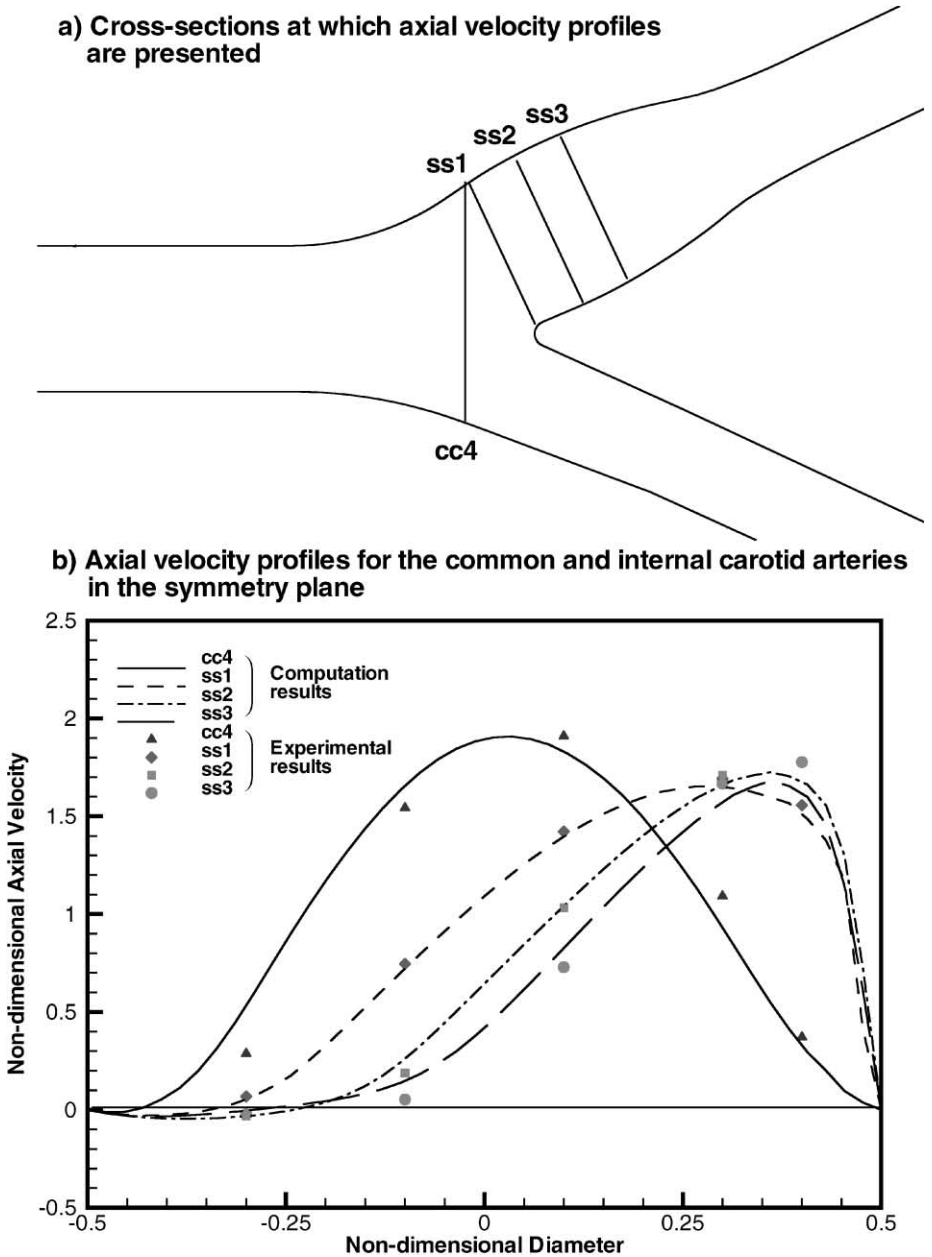

Fig. 4. Validation of axial velocity profiles at different cross-sections in symmetry plane (cf. Bharadvaj et al., 1982) for a reference carotid artery bifurcation.

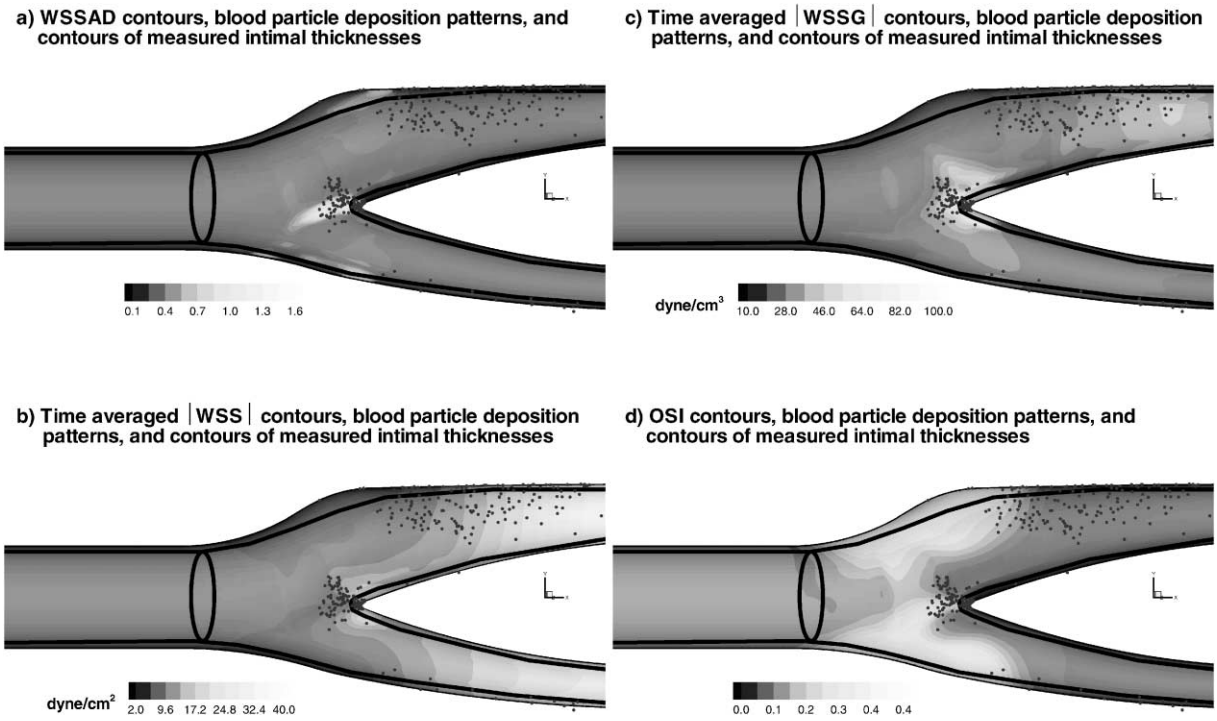

Fig. 5. Disturbed flow indicators with intimal thickness measurements (cf. Zarins et al., 1983) and computational particle deposition patterns for a representative carotid artery bifurcation: (a) wall shear stress angle deviation; (b) wall shear stress; (c) wall shear stress gradient; and (d) oscillatory shear index.

The WSSAD correlates better than other time-averaged "disturbed flow" indicator functions in terms of particle deposition patterns as well as the measured intimal thickness distribution.

3. Results and discussion

For the carotid artery with step expansion due to endarterectomy, Hyun [17] showed that the local impact of "disturbed flow", and hence susceptible sites for the onset of arterial diseases, is best indicated by the WSSAD. Wall deposition patterns of critical blood particles, such as monocytes (i.e., particle diameter $d_p = 14$ μm and density $\rho_p = 1.07\ \mathrm{g/cm^3}$) as well as sites of dysfunctional endothelium are assessed employing the WPD, the WSSG, and the OSI as well. In summary, sustained local changes in wall shear stress vector affecting the endothelial cell morphology and function as well as particle deposition/aggregation represent major *detrimental* hemodynamic factors in the etiology of arterial diseases [4,16,18].

Results are shown for the endarterectomized carotid artery bifurcation (ECAB), a CAB with smoothed step expansion (SCAB), and an idealized design (ICAB). Disturbed flow is illustrated with velocity vector plots as well as the wall shear stress vector distributions at two critical time levels, i.e., peak systole, $t_1 = 0.14$ s, and end of systole, $t_2 = 0.33$ s (cf. Figs. 6–8). The time-averaged

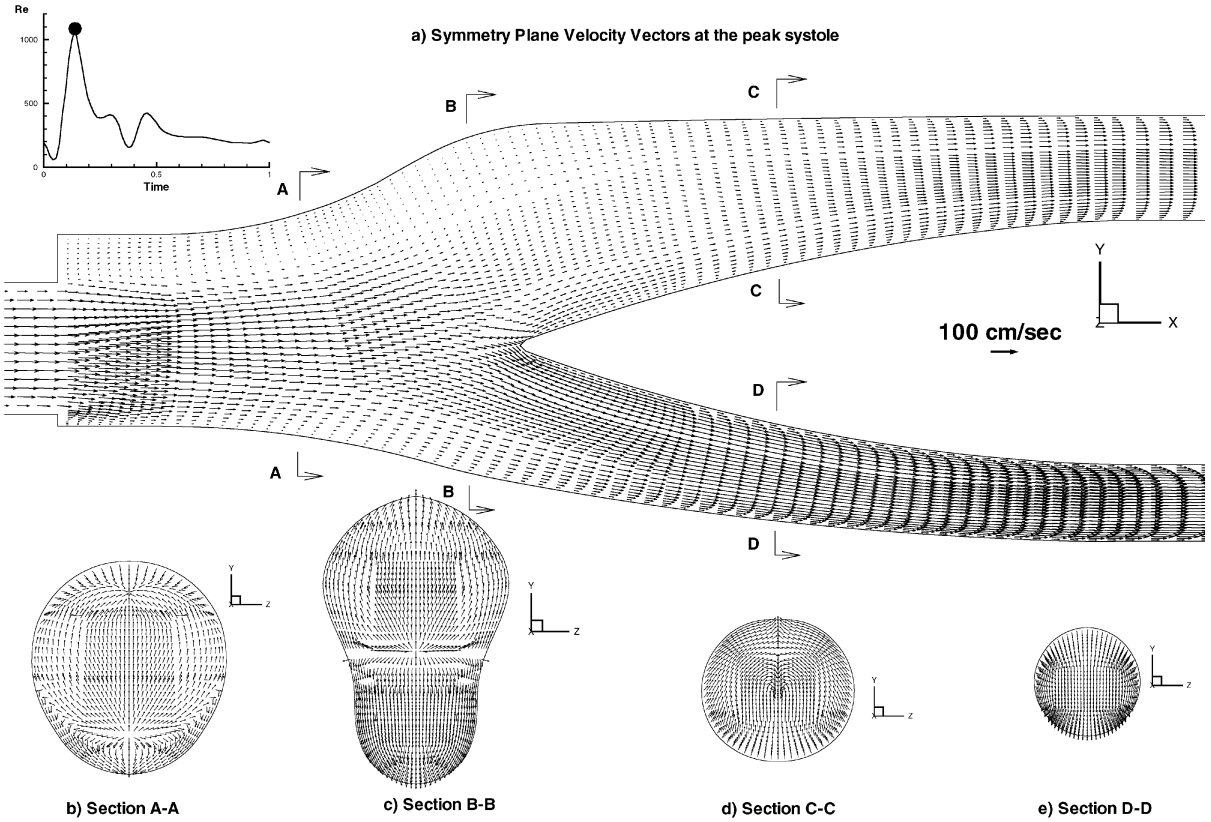

Fig. 6. Transient velocity vector fields in symmetry plane (a) and four cross-sectional secondary velocity fields (b–e) at the peak systolic input pulse for the ECAB.

WSSAD as well as the particle deposition patterns are shown in Figs. 9–11. The final graph, i.e., Fig. 12b, compares the three CAB configurations in terms of segmentally surface area-averaged values of all indicator functions.

3.1. Velocity and wall shear stress vector fields

The upstream step expansion after carotid endarterectomy generates highly vortical flow which in turn produces extended regions of disturbed flow in the junction area as indicated in Figs. 6 and 7 showing velocity fields for the ECAB at two time levels. Specifically, the asymmetric sudden expansion in the common carotid forms centered jetting flows which leads at times to extended zero-flow or strong flow recirculation zones near the expansion wall, especially along the entire upper non-divider wall. Superimposed are secondary velocity fields as depicted in the cross-sectional views of Figs. 6b–e and 7b–e. The impact of the asymmetric expansion is noticeable in the proximal internal and external carotid arteries. The flow characteristics distal to the internal and external carotid arteries are not affected because of the influences of the enlargements in the bifurcating area and subsequently the tapering effect of the distal internal carotid artery (Figs. 6a, c, d and 7a, c, d). Even at the peak

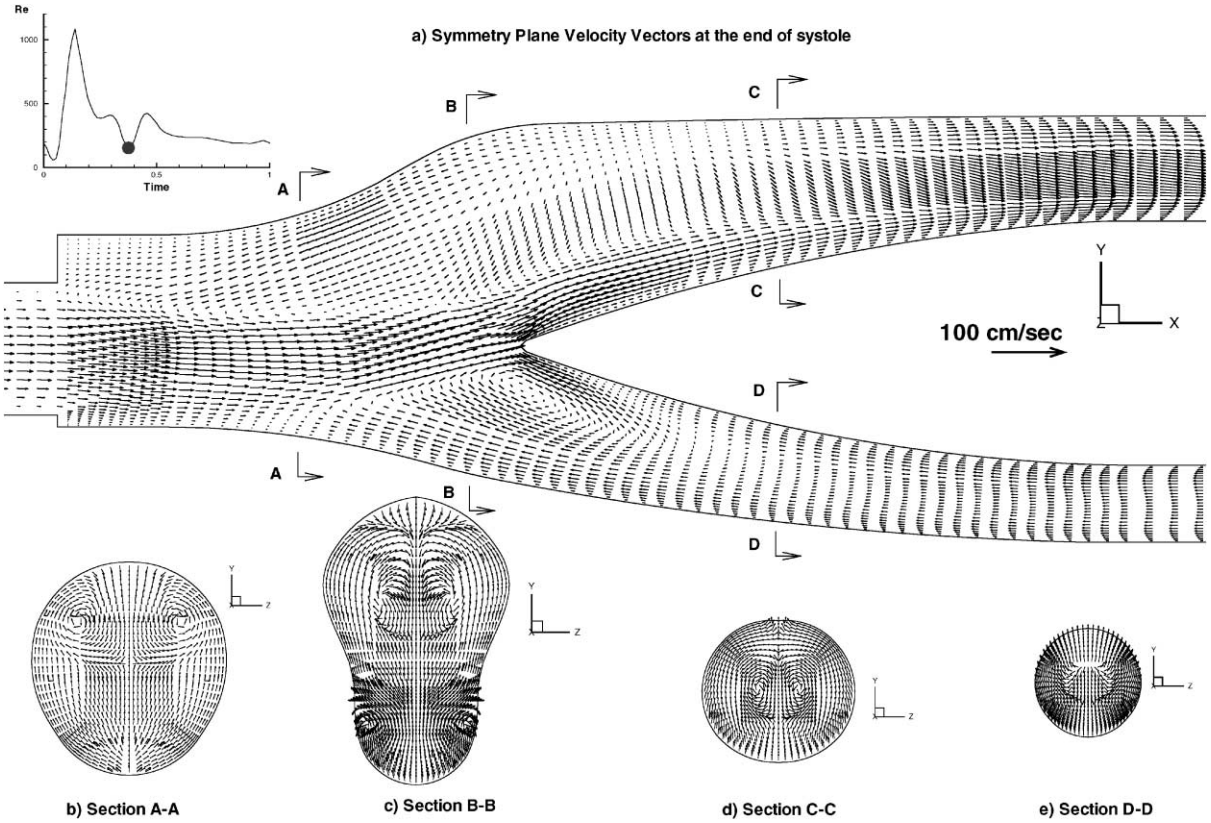

Fig. 7. Transient velocity vector fields in symmetry plane (a) and four cross-sectional secondary velocity fields (b–e) at the end of the systolic input pulse for the ECAB.

systole, reverse flow exists along the non-divider wall in the common and proximal internal carotid arteries. The recirculation region in the carotid sinus is bigger than that for the CAB without partial occlusion [17]. At the end of the systolic phase, i.e., $t = t_2 = 0.33$ s, the external branch experiences reverse flow due to the change in downstream impedance (cf. Fig. 2d). As a result, highly vortical flow appears in the junction area where the incoming stream and the backflow stream meet (cf. Fig. 7a,c).

Temporal variations of WSS magnitude and temporal WSS vector distributions at two time levels are shown for the ECAB in Figs. 8a–d. The level of WSS is lower compared with the unobstructed CAB [17], where no partial occlusion exists in the common carotid. Low WSS regions appear near the expansion wall for both time levels, in the lateral wall in the bifurcation region and the carotid sinus at the peak systole, and in the distal carotid sinus at the end of the systolic input pulse. Due to the asymmetric step expansion, the significant changes in WSS-vector *direction* prevail, and the region between the step expansion and the carotid sinus exhibits low-level WSS values. In summary, the influence of the disturbances generated by the step expansion reaches the proximal carotid sinus and the ECAB has larger surface areas of low WSS-values than an unobstructed CAB.

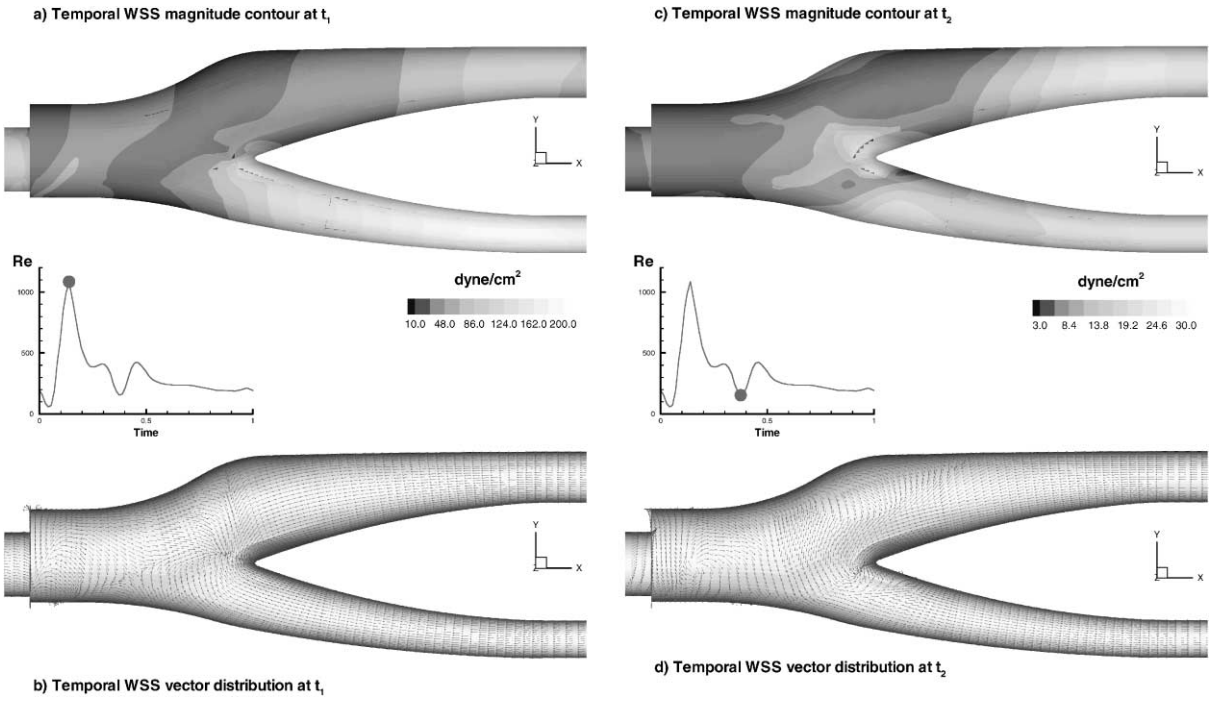

Fig. 8. Temporal WSS magnitude contours and temporal WSS vector distributions for the ECAB.

3.2. Indicator of susceptible sites

As discussed, the WSSAD is employed as the most encompassing indicator function for disturbed flow and hence potential sites of restenosis. In Section 3.3, particle deposition patterns are viewed in support of this underlying hypothesis (cf. Fig. 1).

The 3-D WSSAD surface contours are given in Figs. 9a–c for the three configurations of interest, i.e., the ECAB, SCAB, and ICAB. As expected, sustained elevated WSSAD-values are found near the sudden expansion, in the carotid sinus, and at the junction to the external carotid artery (cf. Fig. 9a). These are areas of highly disturbed flow as evident in secondary fluid motion toward the arterial wall and significant changes in mean wall shear stress vector direction. The first geometric design step was to smooth the 90° step in the common carotid. The actual wall curvature was rather immaterial [17], i.e., a 45° slant was about as good as a higher-order curve. The resulting, somewhat improved WSSAD- distribution for the SCAB is shown in Fig. 9b. The ICAB was designed, based on previous configurations [7,11] and limited clinical observation with patch-reconstructed CABs [27]. Specifically, the step was converted into a long conical expansion and the carotid sinus was basically eliminated. As a result, the WSSAD contours in the ICAB have largely vanished with the exception of a region in the external branch and axially before the divider wall. This is due to the reverse flow in the external carotid for $0.33\ \text{s} \leqslant t \leqslant 0.41\ \text{s}$ (cf. Fig. 2d) and the resulting oscillatory and vortical flow patterns, most sustained in these two regions.

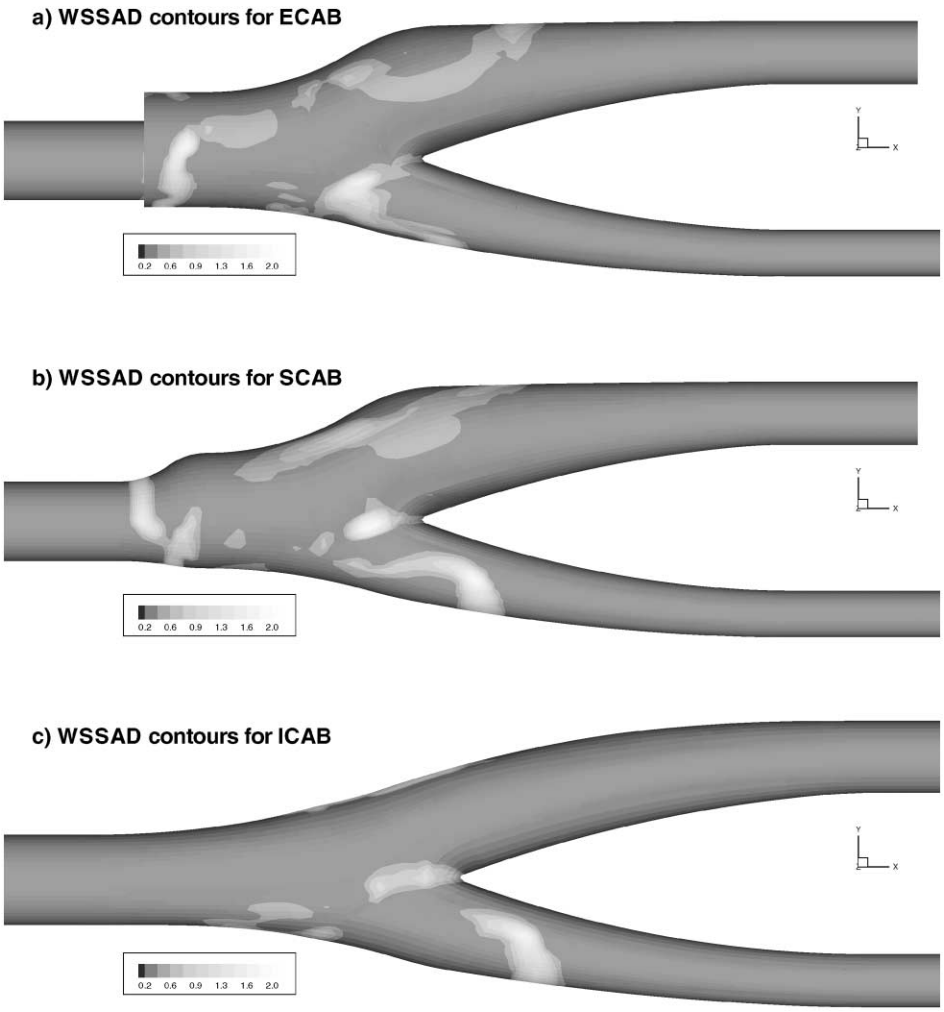

Fig. 9. Three-dimensional surface contours of the WSSAD for: (a) the endarterectomized carotid artery bifurcation; (b) the smooth carotid artery bifurcation; and (c) the idealized carotid artery bifurcation.

3.3. Evolution of particle deposition patterns

Figs. 10a–h present the time evolution of particle dispersion in the ECAB in form of three-dimensional surface projections for a finite volume of particles ($d_p = 14$ μm, $n_{p,in} \approx 10,000$) seeded upstream and then released at $t = 0$ s in the common carotid inlet, representing a volumetric particle pulse or bolus.

Strong vortical flows keep some particles for a prolonged period of time in the junction region and another group of particles is deposited during temporally recirculating flow onto the step expansion wall. The particles seeded around the center of the inlet tube (i.e., the common carotid artery) convect into the expanded junction region and most are washed out of the bifurcation while some

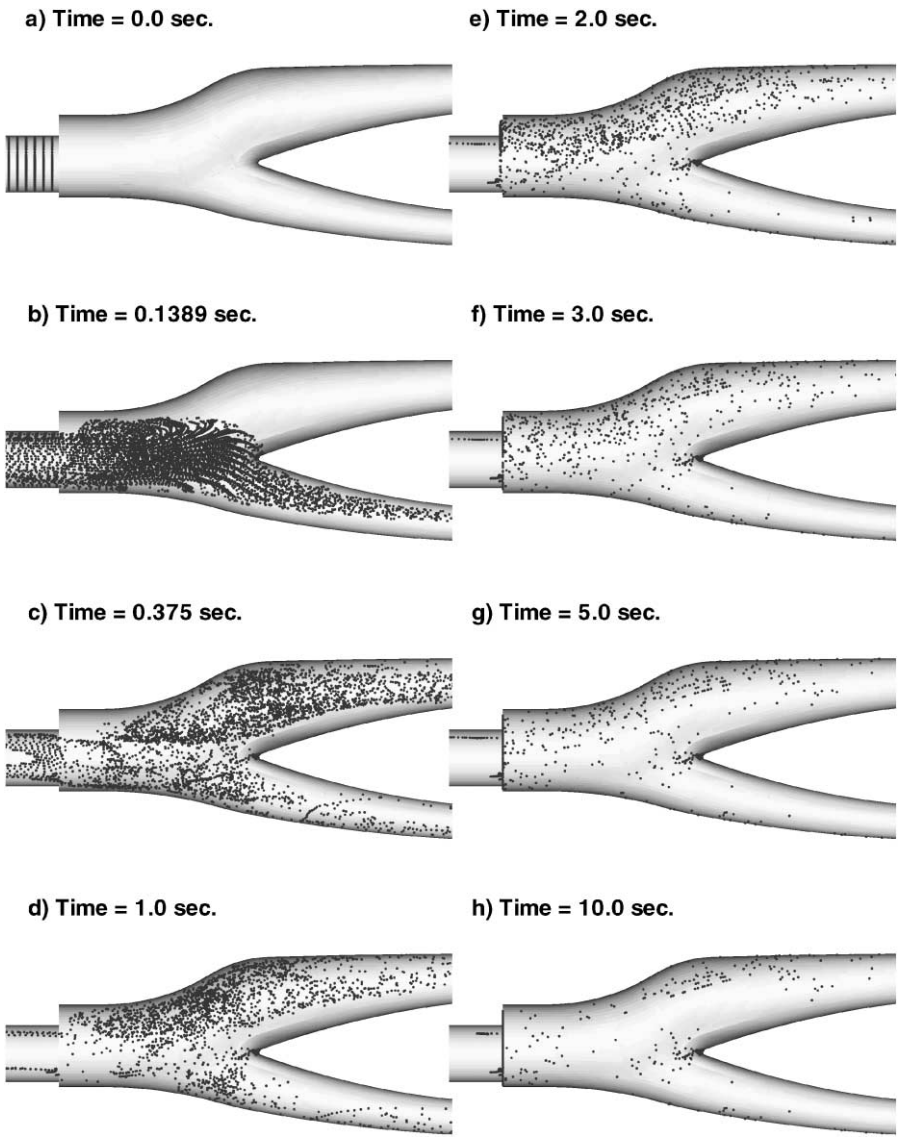

Fig. 10. Time-evolution of particle transport and deposition in the ECAB geometry for a volumetric particle pulse released upstream at $t = 0$ s in the common carotid artery, where $t = 10$ s represents quasi-equilibrium deposition.

are entrained by recirculating flow fields. Surprisingly few particles impact directly on the divider ridge. From the motion of near-wall particles, one can visualize the separating boundary flow and the recirculating flow motion near the step expansion. It could be speculated that the high particle deposition at that site indicates possible thrombi formation, or micro-emboli departure, causing potentially stroke or transient ischemia [27]. The quasi-equilibrium particle deposition patterns for the ECAB differ measurably from those for unobstructed CABs [17]. Nevertheless, the possible particle

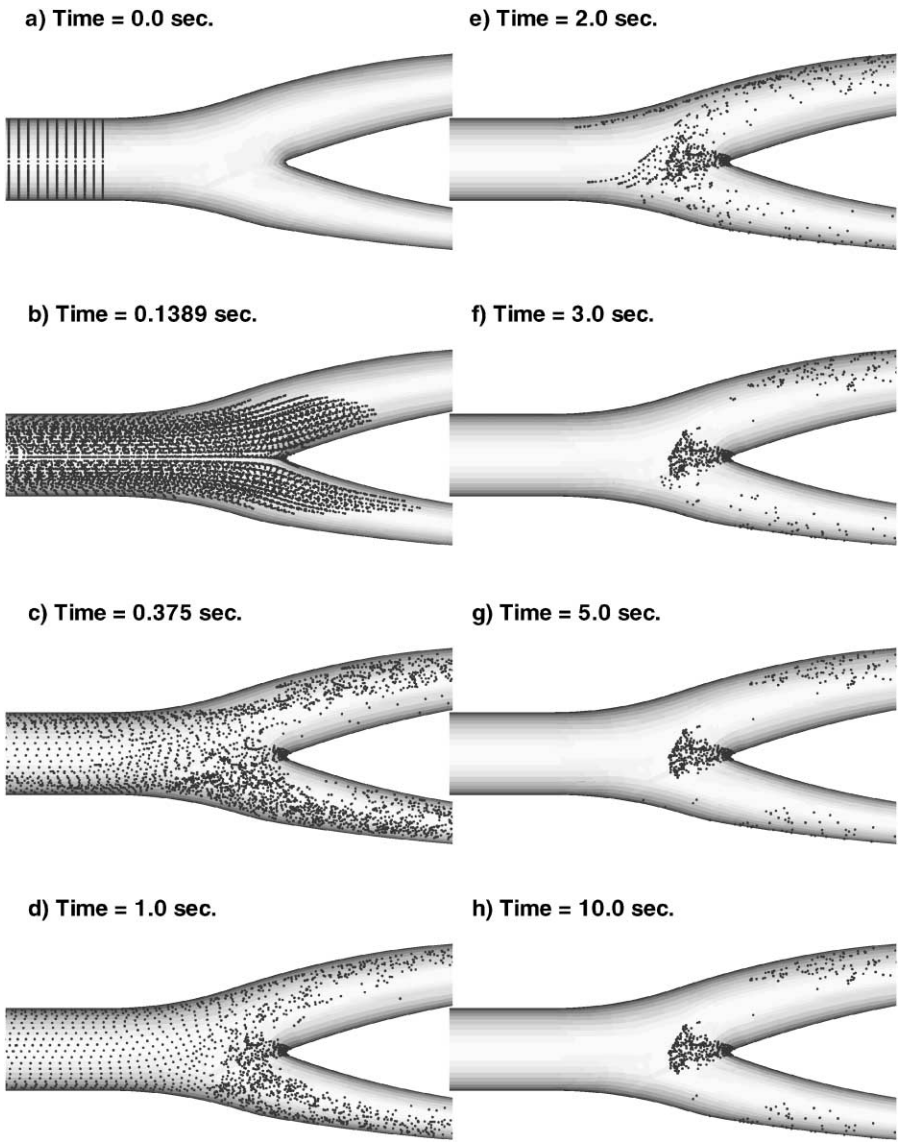

Fig. 11. Time-evolution of particle transport and deposition in the ICAB geometry.

deposition or near-wall aggregation sites are similar to the elevated WSSAD-value regions, which are the regions of the secondary flow toward the wall and the areas of significant changes in WSS-vector direction (cf. Fig. 9a).

The SCAB, being an intermediate solution, has not been considered for critical blood particle transport and deposition. However, the time evolution of particles, starting again with a finite-volume pulse (cf. Fig. 11a), is depicted in Figs. 11b–h for the ICAB. At first the particle bolus splits, impacting more particles onto the divider ridge, and then moves into the branches leaving the inner

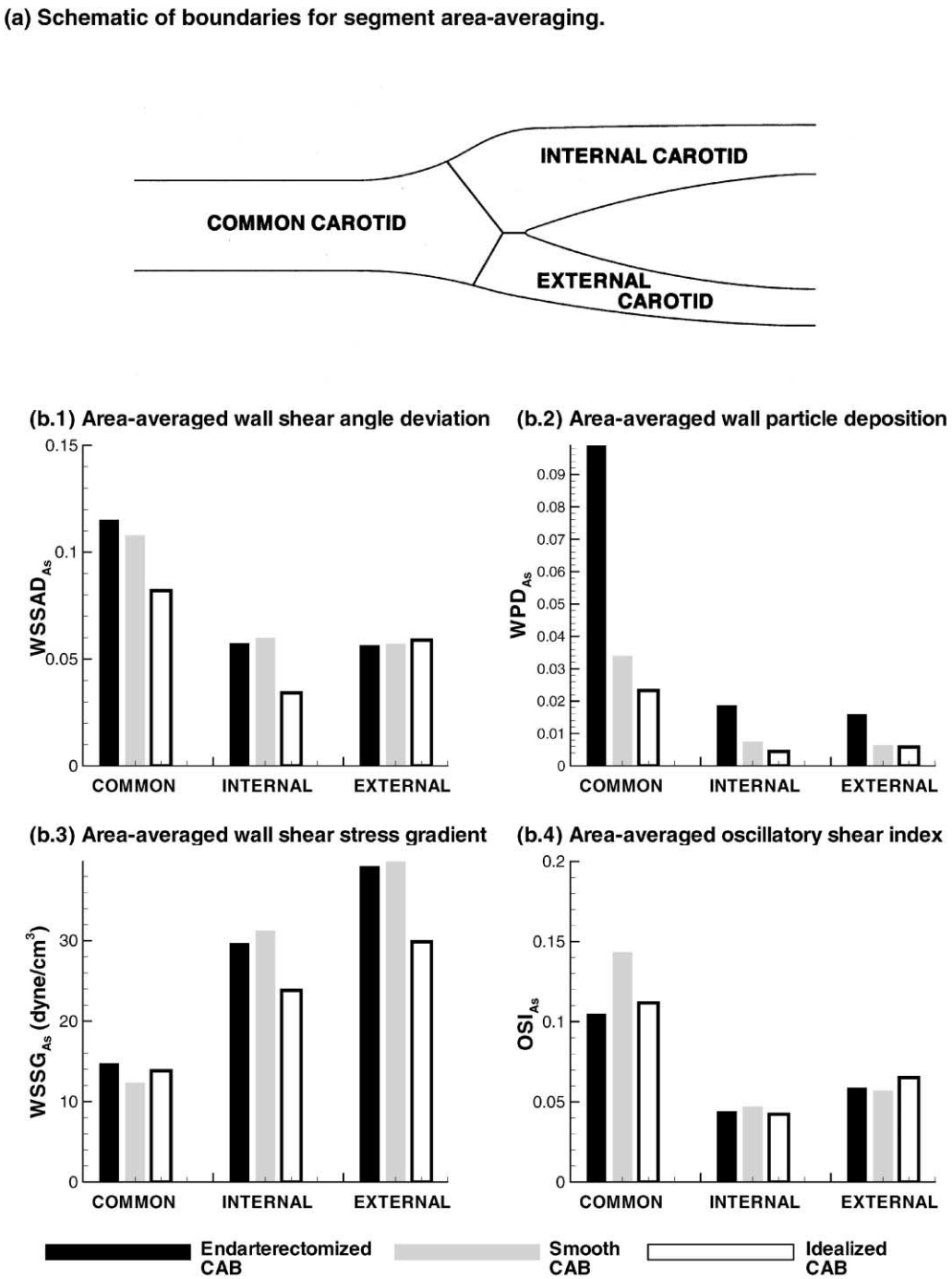

Fig. 12. Segmentally area-averaged indicator functions: (a) schematic of surface boundaries for segment area-averaging; and (b) histograms of four hemodynamic indicators (b.1–b.4).

divider surface areas void of particles, i.e., most of the particles convect downstream following the main flow. However, some particles recirculate slowly in the branches and potentially deposit (cf. Figs. 11e–g). When compared to the ECAB more particles are driven, due to secondary flow, toward the junction side wall before the bifurcation, forming a triangular pattern (cf. Fig. 11h).

3.4. Comparison of CAB configurations

Fig. 12a represents the schematic area-averaging surface boundaries. Three regions are defined as common carotid, internal carotid, and external carotid. The region near the divider wall is shared by the internal and external carotid arteries. Although the system compartmentalization appears to be somewhat arbitrary, the subdivisions and relative comparisons are consistent for all three configurations. Now, averaging the combined disturbed flow indicator functions—WSSAD, WPD, WSSG, and OSI—sequentially over equivalent surface areas of the three bifurcations allows for a relative "performance" comparison of the three CABs (cf. Fig. 12b). Focusing on the WSSAD as the assumed best indicator function, the idealized CAB is a measurable improvement over the endarterectomized CAB as well as the smooth CAB except in the external segment. The normalized equilibrium WPD_{A_s} values (Fig. 12b.2) echo this trend. Specifically, for the endarterectomized step CAB (ECAB), the maximum deposition appears in the common carotid artery. Due to the sudden expansion in the common carotid artery, a large number of particles is deposited in the step expansion area and could be the origin of thrombi formation and particle re-entrainment (cf. Fig. 10). The WSSG (Fig. 12b.3) and OSI (Fig. 12b.4) histograms are of interest as well. Area-averaging of the WSSG in the common carotid smears out the very high WSSG-peaks at the 90°-step and smooth expansions so that the WSSG_{A_s} appears to be comparable for all three configurations. Similar to the WSSD_{A_s} and WPD_{A_s} bar graphs, both the WSSG_{A_s} and the OSI_{A_s} indicate that the external carotid artery of the ICAB design may require improvement. Indeed, for this study, we were considering only the common and internal carotid arteries for design modifications because they are historically prone to failure.

Overall, the idealized carotid artery bifurcation (ICAB) is expected to have a lower probability for restenosis and may even prevent post-operative complications after carotid endarterectomy. However, particle depositions still appear on the lateral wall near the flow divider as a result of the Dean flow effect, on the divider ridge by particle impaction, and downstream in both branches due to the tubular convergence. Thus, more detailed studies on particle transport near arterial walls including particle rolling, slip, as well as restitution are required in the future.

4. Conclusions

The transient three-dimensional fluid-particle flow fields in three different carotid artery bifurcations with common physiological inlet and outlet geometries as well as input and outflow waveforms have been computationally investigated. Velocity vector fields have been visualized, and disturbed flow indicators, i.e., the wall shear stress angle deviation (WSSAD), wall particle deposition (WPD), wall shear stress gradient (WSSG), and oscillatory shear index (OSI) have been calculated, compared and discussed.

The WSSAD has proven to be a suitable indicator of disturbed flow and hence for the prediction of the onset of arterial diseases in the endarterectomized carotid artery bifurcation. The regions with

elevated WSSAD-values cover the areas of very low and very high WSS, as well as directional WSS-vector changes. In support of the WSSAD, the WPD represents local surface areas of potential particle deposition. High WSSAD values appear at the divider wall which is characterized by very high WSS and elevated WSS gradient values, and at the distal carotid sinus which is characterized by very low WSS and elevated oscillatory WSS values. Possible particle depositions, or at least prolonged near-wall residence times, are observed in these arterial regions as well, recognized by the disturbed flow indicator WSSAD and quantitatively captured by the WPD.

Using the WSSAD as a key indicator for the disturbed flow, a geometrically improved carotid artery bifurcation (ICAB) was developed which may mitigate the probability of thrombus formation and recurrent stenosis related to non-uniform hemodynamics. Geometric variations in finite length of the step-down did not help to improve the reconstruction of the endarterectomized carotid artery bifurcation significantly [26–28]. It is recommended that a longer conical change, if at all possible, without any inflection point is considered for improvements in arterial reconstructions. Overall, a significant reduction of WSSAD- and WPD-values were achieved by eliminating the carotid sinus.

Even though the combined hospital mortality and non-fatal stroke rate is generally less than 7%, the imperfections of carotid endarterectomy and prevailing disturbed flow patterns may lead to stroke. Therefore, the recommendations for surgical reconstruction presented merit consideration.

Acknowledgements

The authors wish to acknowledge AEA Technology (Bethel Park, PA), SGI/Cray (Eagan, MN), NIH (Bethesda, MD) and MCNC/NCSC (RTP, NC) for their support.

References

[1] J.L. Mills, R.M. Fujitani, S.M. Taylor, The characteristics and anatomic distribution of lesions that cause reverse vein graft failure: a five-year prospective study, J. Vascular Surg. 17 (1) (1993) 195–204.

[2] J.P. Archie Jr., The endarterectomy-produced common carotid artery step: a harbinger of early emboli and late restenosis, J. Vascular Surg. 32 (5) (1996) 932–939.

[3] C. Kleinstreuer, S. Hyun, J.P. Archie Jr., Computer-aided design and optimal surgical reconstruction of the carotid artery bifurcation, in: T.B. Martonen (Ed.), Medical Applications of Computer Modeling: Cardiovascular and Ocular Systems, WIT Press, Southampton, UK, 2000.

[4] C. Kleinstreuer, S. Hyun, Computer simulation of dilute suspension flows in branching blood vessels, in: T.B. Martonen (Ed.), Medical Applications of Computer Modeling: Cardiovascular and Ocular Systems, WIT Press, Southampton, UK, 2000.

[5] S. Hyun, C. Kleinstreuer, J.P. Archie Jr., Computer simulation and geometric design of endarterectomized carotid artery bifurcations, 18th Southern Biomedical Conference, May 20–3, 1999, Clemson, SC, (S. Saha, Conference Chair), Also: Crit. Rev. Biomed. Eng. 28 (1–3) (2000) 53–59.

[6] B.K. Bharadvaj, R.F. Mabon, D.P. Giddens, Steady flow in a model of the human carotid bifurcation. Part II—laser-Doppler anemometer measurements, J. Biomech. 15 (5) (1982) 363–378.

[7] D.R. Wells, J.P. Archie, C. Kleinstreuer, Effects of carotid artery geometry on the magnitude and distribution of wall shear stress gradients, J. Vascular Surg. 23 (4) (1996) 667–678.

[8] K. Perktold, G. Rappisch, M. Hofer, D. Liepsch, Flow characteristics in an anatomically realistic compliant carotid artery bifurcation model, Bioengineering Conference, ASME BED 29 (1995) 405–406.

[9] D.N. Ku, D.P. Giddens, C.K. Zarins, S. Glagov, Pulsatile flow and atherosclerosis in the human carotid bifurcation: positive correlation between plaque location and low and oscillating shear stress, Atherosclerosis 5 (1985) 293–302.

[10] K. Perktold, R.O. Peter, M. Resch, G. Langs, Pulsatile non-Newtonian blood flow in three-dimensional carotid bifurcation models: a numerical study of flow phenomena under different bifurcation angles, J. Biomed. Eng. 13 (1991) 507–515.
[11] C. Kleinstreuer, M. Nazemi, J.P. Archie Jr., Hemodynamics analyses of a stenosed carotid bifurcation and its plaque-mitigating design, ASME J. Biomech. Eng. 113 (3) (1991) 330–335.
[12] C. Kleinstreuer, Engineering Fluid Dynamics—An Interdisciplinary Systems Approach, Cambridge University Press, New York, 1997.
[13] R.A. Macosko, Rheology: Principles, Measurements, and Applications, VCH Publications, New York, 1994.
[14] E.W. Merrill, Rheology of blood, Physiol. Rev. 49 (4) (1969) 863–888.
[15] J.R. Buchanan Jr., C. Kleinstreuer, Simulation of particle-hemodynamics in a partially occluded artery segment with implications to the initiation of microemboli and secondary stenosis, J. Biomech. Eng. 120 (1998) 446–454.
[16] C. Kleinstreuer, S. Hyun, J.R. Buchanan, P.W. Longest, J.P. Archie, G.A. Truskey, Hemodynamic indicator functions of susceptible sites of early intimal thickening in branching blood vessels, Crit. Rev. Biomed. Eng. 29 (2001).
[17] S. Hyun, Transient particle-hemodynamics simulations in three-dimensional carotid artery bifurcations, Ph.D. Dissertation, North Carolina State University, Raleigh, NC, 1998.
[18] J.R. Buchanan Jr., C. Kleinstreuer, G.A. Truskey, M. Lei, Relation between non-uniform hemodynamics and sites of altered permeability and lesion growth at the rabbit aorto-celiac junction, Atherosclerosis 143 (1999) 27–40.
[19] J.R. Buchanan Jr., S. Hyun, C. Kleinstreuer, G.A. Truskey, Local monocyte deposition patterns and elevated permeabilities in the rabbit abdominal aorta, Biomedical Engineering Annual Meeting, Big Sky, Montana, June 16–19, BME Society, 1999.
[20] S.V. Patankar, Numerical Heat Transfer and Fluid Flow, Hemisphere, Washington, 1980.
[21] J.S. Milner, J.A. Moore, B.K. Rutt, D.A. Steinman, Hemodynamics of human carotid artery bifurcation: computational studies with models reconstructed from magnetic resonance imaging of normal subjects, J. Vascular Surg. 27 (1998) 143–156.
[22] J.R. Buchanan Jr., Computational analysis of particle-hemodynamics in stenosed artery segments, MS thesis, Department of Mechanical and Aerospace Engineering, North Carolina State University, Raleigh, NC, 1996.
[23] J.K. Comer, Computational two-phase flow analyses and applications to gas–liquid and gas–solid flows, Ph.D. Dissertation, Mechanical and Aerospace Engineering Department, North Carolina State University, Raleigh, NC, 1998.
[24] P.W. Longest, Computational hemodynamic simulations and comparison studies of AV-access grafts for hemodialysis, MS Thesis, Department of MAE, North Carolina State University, Raleigh, NC, 1999.
[25] C.K. Zarins, D.P. Giddens, B.K. Bharadvaj, V.S. Sottiurai, R.F. Mabon, S. Glagov, Carotid bifurcation atherosclerosis: quantitative correlation of plaque localization with flow velocity profiles and wall shear stress, Circulation Res. 53 (1983) 502–514.
[26] J.P. Archie, Geometric dimension changes with carotid endarterectomy reconstruction, J. Vascular Surg. 25 (3) (1995) 488–498.
[27] J.P. Archie, The endarterectomy-produced common carotid artery step: a harbinger of early emboli and late restenosis, J. Vascular Surg. 32 (5) (1996) 932–939.
[28] S. Hyun, C. Kleinstreuer, J.P. Archie, Hemodynamics analyses of arterial expansions with implications to thrombosis and restenosis, Med. Eng. Phys. 22 (2000) 13–27.

Sinjae Hyun obtained his Ph.D. degree in Mechanical Engineering from North Carolina State University (NCSU) in 1998 and MS and BS degrees in Mechanical Engineering from Kyungpook National University, Korea, in 1986 and 1988, respectively. He was a Research Engineer at the Division of Propulsion System, ADD, Korea from 1988 to 1994. Dr. Hyun was a Research Associate from 1999 to 2000 and is presently a Research Assistant Professor in the Department of Mechanical and Aerospace Engineering at NCSU. His research interests are in the areas of computational particle-fluid dynamics simulations applied to hemodynamics in arterial junctions and pollutant transport in human inhalation test chambers and heat transfer enhancement in micro-systems.

Dr. Clement Kleinstreuer is a Professor in the Department of Mechanical and Aerospace Engineering at NC State University, Raleigh, NC. He received his Ph.D. from Vanderbilt University. He has published over 90 refereed journal articles, eight book chapters, and

one graduate-level text. His research area is computational fluid-particle dynamics with applications to biomedical engineering and microfluidics.

Dr. Joseph P. Archie is a Vascular Surgeon at Wake Medical Center in Raleigh, NC. He received his Ph.D. in Engineering Mechanics from NC State University and his MD from the University of North Carolina, Chapel Hill. As a surgeon, he specializes in carotid endarterectomy and femoral bypass operations. As an engineer and research MD, he collaborates with Prof. Kleinstreuer's group on optimal reconstruction of carotid artery bifurcations and optimal designs of graft-to-artery anastomoses. His numerous contributions have appeared in top journals of vascular surgery and biomedical sciences.